Microstructural Modification of Laser-Deposited High-Entropy CrFeCoNiMoWC Alloy by Friction Stir Processing: Nanograin Formation and Deformation Mechanism

CrossMark

RUIDI LI, MINBO WANG, TIECHUI YUAN, BO SONG, and YUSHENG SHI

Nanostructured CrFeCoNiMoWC high-entropy alloy layer was developed through laser-melting deposition and severe plastic deformation (SPD). The laser-deposited CrFeCoNiMoWC alloy consists of dendritic and subeutectic with a continuous network structure. After SPD, the laser-deposited microstructure with grain size 3 to 4 μm was transformed into nanostructure with grain size 5 to 100 nm and the continuous networks were crushed into dispersed nanoparticles. The new phases of WC and Co_3W were presented in the plastic zone after SPD due to the worn debris of the SPD tool. More interestingly, amorphous phase was found in the plastic zone, owing to the high temperature, high hydrostatic pressure, and large shear stress. The refined microstructure resulted in the enhancement of microhardness and electrochemical corrosion property. Many nanotwins were detected in the plastic zone; thus, strengthening mechanisms were reasonably inferred as twinning strengthening, work hardening, dispersion strengthening, refinement strengthening, and dislocation strengthening. The Lomer–Cottrell lock, full dislocation interacting with a partial dislocation at the twinning boundary, and high density of dislocation at the twinning boundary, stacking fault, and grain boundary were observed, which account for the property enhancement of the nanocrystalline.

I. INTRODUCTION

IN most conditions, metal failures occur on the surface in the forms of abrasion, fatigue fretting, crack, and corrosion, which seriously decrease the reliability of metal during its service in harsh circumstances, such as the surface wearout of the steam turbine blade under strong alternating stress and corrosion conditions. It is well known that the surface failures rely highly on the strength and microstructure of the surface. For many metal materials, low surface strength and poor wear properties are significantly hindering their engineering application. Consequently, microstructural modification on the surface is an ideal means to enhance the service lifetime and safe reliability of metals.

It is common knowledge that the ultrafine grain or nanograin favors the mechanical properties from the Hall–Petch formulation. Metals could be refined to nanograin by severe plastic deformation (SPD) on the surface with gradient variation from Nano to micro.[1,2] Optimization of surface strengths by surface nanocrystallization can widen the application foreground. At present, nanograin metals, such as Al, Ni, Cu, Ti, Co, and Fe base alloy, have been made by SPD.[3] Nevertheless, the traditional SPD methods, such as high-pressure torsion (HPT)[4] and accumulative rolling bonding,[5] could not enable the surface nanocrystallization and the deformation of high-strength metals. Surface mechanical attrition treatment (SMAT)[6] is a developed technique that can enable surface nanocrystallization via random and repetitive impact of milling balls onto the surface. However, SMAT suffers from low processing efficiencies, limited nanostructure, and microstructural inhomogeneity due to its insufficient material flowability, which have hindered its widespread application.[7,8] Different from other SPD process, friction stir processing (FSP) can create surface microstructure containing ultrafine grains or nanograins with large grain boundary (GB) misorientations, features that are important for enhanced properties.[9,10] FSP is based on the fundamental concepts of friction stir welding by which a rotary tool is inserted into the workpiece, produces friction heat, and then plasticizes the material.[11,12] Thus, FSP has been used as a unique thermomechanical process by which the large plastic strain and temperature lead to smaller grains and breakup of the constituent second phase.[12–14]

Recently, increasing attention has been paid to the research and development of high-entropy alloys (HEAs), in which five or more elements are mixed in

RUIDI LI, MINBO WANG, and TIECHUI YUAN are with the State Key Laboratory of Powder Metallurgy, Central South University, Changsha, 410083, P.R. China. Contact email: liruidi@csu.edu.cn, tiechuiyuan@csu.edu.cn BO SONG and YUSHENG SHI are with the State Key Laboratory of Materials Processing and Die & Mould Technology, Huazhong University of Science and Technology, Wuhan, 430074, P.R. China.

near-equimolar rations, such that the high configurational entropy of mixing could promote solution formation.[15,16] Consequently, HEAs possess several unique characteristics, such as high entropy, sluggish diffusion, lattice distortion, and cocktail effects, which enable various attractive material properties, including good wear resistance, excellent corrosion resistance, outstanding strength, high hardness, and superoxidation resistance.[17,18] Although the first publication appeared not quite 10 years ago, HEAs are being considered to have important applications prospects. So far, most of the studies of HEAs have been concerned with the casting microstructure and properties and only a limited number of studies have focused on the application in surface modification.[19] Laser-melting deposition (LMD) technologies, which were characterized as its flexible shaping control, fine microstructure, and widespread applications, have been widely used in surface processing and additive manufacturing.[20–23] The preparation of HEAs by LMD is meaningful. First, LMD could yield complex shapes of HEAs, while conventional methods could not. Second, LMD enables HEAs with nonequilibrium microstructures, which exhibit uniform properties compared to the equilibrium microstructure. Based on the preceding considerations, the laser deposition was chosen to evaluate its potential for HEA synthesis, such as the fabrication of Ti,[24] Fe,[25] Al,[26] Cu,[27] and Ni[28] HEAs by laser melting. The LMD HEAs are usually accompanied with metallurgy defects such as constitute brittle phase and as-formed intercrystalline crack. Moreover, the microstructure of LMD HEAs usually exhibits dendritic grain with several micrometers, which is coarser compared with the SPD-processed nanostructure. Therefore, refining the microstructure of LMD HEAs by SPD is regarded as necessary and interesting, and mechanical strength is expected to be enhanced. There is little previous literature about SPD of HEAs. Schuh et al.[29] prepared nanocrystalline CoCrFeMnNi HEAs by HPT and evaluated their microstructure, property evolutions, and high-temperature stability. Similarly, Tang et al.[30] produced nanostructured Al0.3CoCrFeNi HEAs by HPT subjected on a cast part and found that HPT combined with annealing improved its hardness. Yuan et al.[31] investigated the atomic-scale homogenization of fcc-based HEAs via casting and SPD. Previous literature mainly focused on HPT of HEAs.

To the best knowledge of the authors, studies on the production of nanostructured HEA surface layers, especially by the FSP method, are few. In the present work, the CrFeCoNiMoWC HEA was selected to evaluate its microstructure and performances by LMD and FSP. The selection of this CrFeCoNiMoWC alloy was due to its well wetting and flowing abilities, which are suitable for laser deposition. Moreover, the CrFeCoNiMoWC HEA has great potential for a wide range of hardfacing applications, such as turbine blades, vanes, combustion systems, and valve trims. The nanostructured CrFeCoNiMoWC HAE surface layer was prepared by a combination of LMD and FSP for the first time. The nanograin formation, microstructural evolution, and mechanical properties were characterized and their deformation mechanisms were also illuminated.

II. EXPERIMENTAL PROCEDURE

A. *LMD of CrFeCoNiMoWC Powder*

The nominal chemical compositions of the gas-atomized CrFeCoNiMoWC alloy powder in mass fraction, wt pct (mole fraction, at. pct), were Cr: 28.79 (31.05), Fe: 28.20 (28.24), Co: 14.56 (13.84), Ni: 11.50 (10.93), Mo: 5.81 (3.39), W: 6.33 (1.93), and C: 2.27 (10.61). The substrate used for LMD was an A3 steel with dimensions 50 mm × 70 mm × 10 mm. Before laser deposition, the surface was ground using a 400-μm grit paper and was sand blasted to decrease surface reflectivity. Afterward, the CrFeCoNiMoWC powder was deposited onto the surface of the substrate with a thickness of about 1.0 to 1.5 mm. The LMD machine was equipped with a 5-kW pulsed CO_2 laser (λ = 10.06 μm) and a three-axes numerically controlled working station. During the LMD process, a Gaussian pulse laser with a stable circular spot was used and the molten pool was filled with Ar gas to avoid oxidation with a flow rate of 25 L/min. The spot size of the laser beam was about 4 mm on the steel substrate. The dilution ratio was below 10 pct. The laser power and scan speed govern the energy density, which ultimately determines the molten pool depth, width, and spread properties. The overlap ratio correlates with the solidification stress, crack, and surface roughness. Based on the preceding factors, the laser parameters were optimized with the aim of obtaining a crack-free and nonporous surface. The optimized laser parameters were as follows: laser power 2 kW, scanning speed 5 mm/s, and overlapping ratio 30 pct.

B. *FSP on the Laser-Clad CrFeCoNiMoWC Layer*

After LMD, the CrFeCoNiMoWC coating was modified by FSP. However, the FSP tool is very easily worn out owing to the high hardness, wear resistance, and high melting point of the CrFeCoNiMoWC alloy. Therefore, in the present work, the FSP tool was made by WC-Co hard alloy rod without a probe with diameter 12 mm. The total LMD and FSP routes are schematically illustrated in Figure 1. The FSP was completely carried out in the laser-deposited CrFeCoNiMoWC alloy. During FSP, the high-speed spinning tool inserted into the laser coating and then moved along a direction forming friction heat and severe shear deformation. The change of rotation speed affects the heat input, the temperature filed, and the resultant micro- or nanostructure. Usually, the travel speed is changed to balance the heat input rise from the increase in the rotation speed. When FSP was at a high rotation or travel speed specific value, the friction tool was easily worn. However, when the rotation or travel speed specific value was too low, the plastic zone was hardly formed. The FSP parameters were changed rotation speed 300 to 1500 rpm and constant travel speed 10 mm/min. During FSP,

the tool was tilted 3 deg toward the backside with respect to the surface normal.

C. Evaluation of the LMD and Laser-FSP CrFeCoNiMoWC Layer

Phase identification of the LMD coating before and after FSP was conducted by D/max2500pc X-ray diffraction (XRD) with Cu K_a radiation ($k = 0.154$ nm). Samples were cut, ground, and polished from a cross section according to the standard procedures for metallographic observations and then etched with a solution consisting of H_2O_2, HCl, and methanol for 10 to 30 seconds. The microstructural evolution of LMD HEA coating before and after FSP was detected with a scanning electron microscope (SEM, Nova Nano SEM 230) equipped with an energy-dispersive spectrum (EDS). The EDS quantitative analysis was calibrated by zeta zat, X-ray absorption, and fluorescence. The element composition was also corroborated with an electron-probe microanalyzer (EPMA, JXAe8530, JEOL*). In order to further observe the

---

*JEOL is a trademark of JEOL, Tokyo.

---

nanostructure of the deformed zone, a transmission electron microscope (TEM) specimen was extracted from the cross section of the coating surface by focused ion beam (FIB FEI Helios nanolab 600) "lift-out" technology. Then the FIB specimen was observed with a TEM (JEOL-2100F) operating at 200 kV and a high-resolution transmission electron microscope (HRTEM) equipped with a selected area electron apparatus. The microhardnesses of CrFeCoNiMoWC layers were tested with a micro-Vickers hardness tester with a load of 300 g for 10 seconds (ASTM E384-08). The electrochemical corrosion behaviors of CrFeCoNi MoWC alloy before and after FSP were studied using potentiodynamic polarization. A conventional three-electrode cell assembly was used for electrochemical measurements, with a saturated calomel electrode as the reference electrode and a platinum foil as the auxiliary electrode. Potentiodynamic polarization scans were carried out with a scan rate of 1 mV per second. The potential range measured was from –0.15 to 0.15 V.

III. RESULTS AND DISCUSSION

A. Microstructure of LMD CrFeCoNiMoWC Alloy

The typical microstructures of LMD CrFeCoNi MoWC alloy at different magnifications are shown in Figure 2. The microstructures of the laser-deposited alloy are mainly composed of dendritic and subeutectic structures with crystallite dimension of about 3 to 4 μm. The interdendritic eutectic formed a continuous structure. The EDS analyses of this microstructure were conducted to determine the chemical compositions of the primary phase and the subeutectic, as shown in Figures 2(d) through (f). Different elemental compositions exist, as indicated by joint spiders A and B (Figure 2(d)). The EDS results showed that the carbon content in the interdendritic zone was higher than that in the dendritic zone. However, the EDS resolution is limited owing to the fine dendritic grain. Thus, the elemental composition was analyzed by integration of EPMA, as shown in Figure 3. It can be found that the elements C, Cr, Mo, and W are rich in the interdendritic zone, while Fe, Co, and Ni are rich in the dendritic zone. Thus, it can be concluded that the carbides are precipitated along the GB during the solidification process. During the LMD process, primary dendrites grow epitaxially on the molten pool boundary. With the gradual decrease of temperature, solute dissolved out from the solidification front combined with the formation of second phase or eutectic with low melting points. When the growing dendrites collided, the second phase and eutectic with enriched solute atoms were residual in the dendritic GB, forming the continuous networks. Note that the continuous networks can lead to the intergranular crack easily during solidification, owing to the tensile stress acting on the intergranular residue liquid at the final stage of solidification. In addition, the continuous networks are brittle, which also favors crack initiation (Figure 2(c)). Except for the laser-deposited
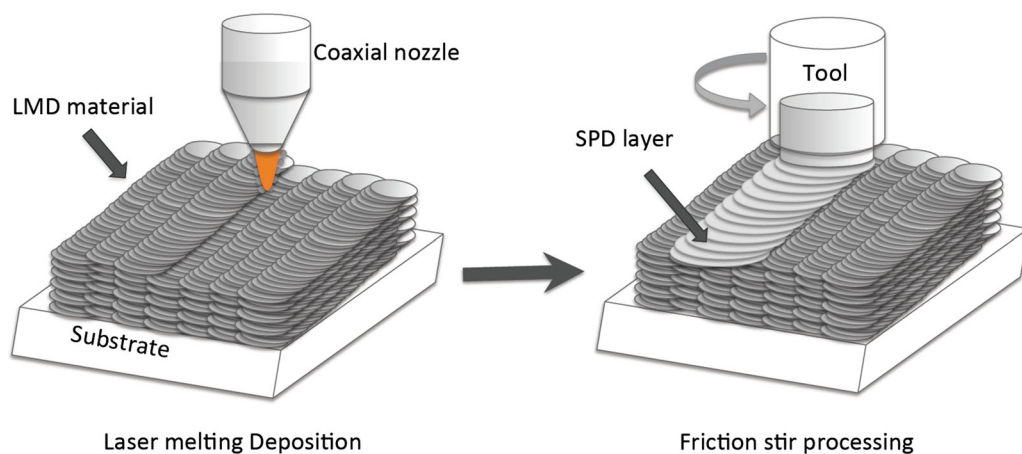

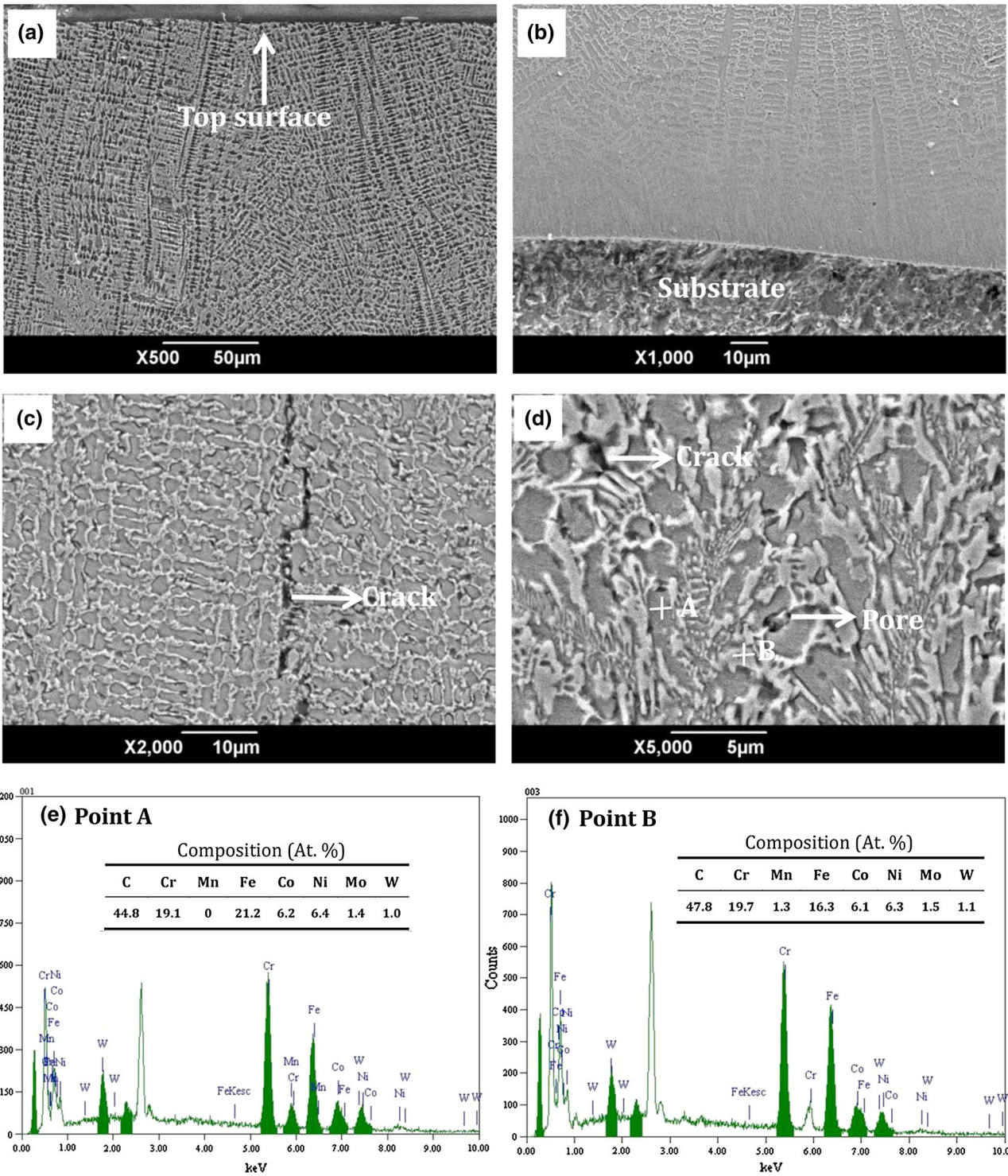Fig. 1—Schematic diagram showing the LMD and FSP process.

Fig. 2—SEM images showing the typical microstructure of LMD CrFeCoNiWMoMnC alloy: (*a*) upward section, (*b*) downward section, (*c*) crack initiation along the GB, (*d*) dendritic and subeutectic structures, (*e*) spectrum of point A, and (*f*) spectrum of point B.

HEAs, the networks precipitating in the GB is a common phenomenon and usually presents in other laser-melted alloys, such as Al-base,[32] Fe-base, Ni-base,[33] and Co-base alloy.[34] Therefore, adjusting the networks to uniformly dispersed nanoparticles in solution and improving their comprehensive properties are necessary, which will be investigated in Section III–B.
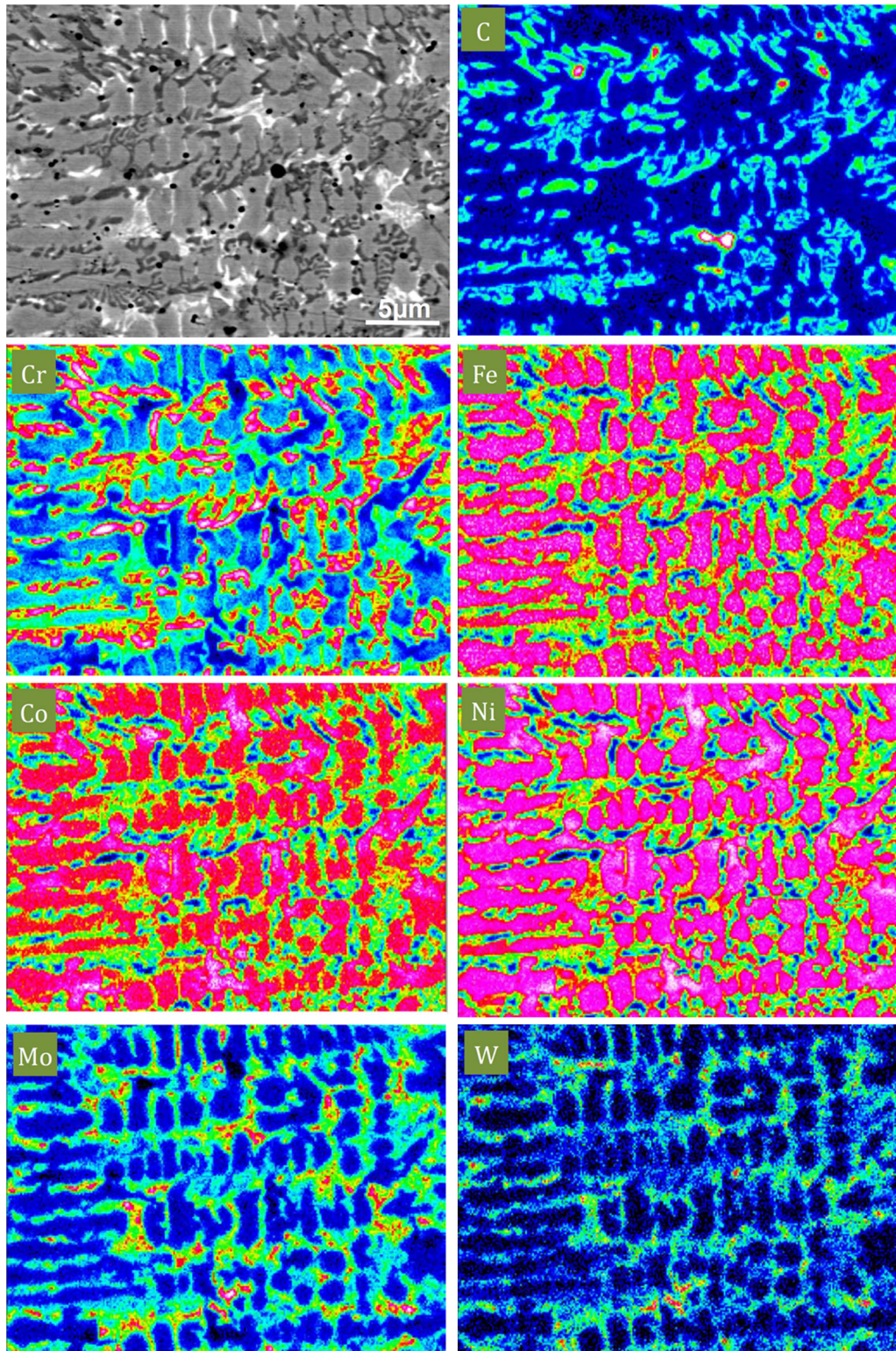
Fig. 3—EPMA element maps of the LMD CrFeCoNiWMoMnC alloy.

B. Nanostructured CrFeCoNiMoWC Layer Fabricated by FSP on the LMD Surface

Figure 4 shows the XRD patterns of the laser-melted CrFeCoNiMoWC alloy layer before and after FSP using different rotary speeds. It can be seen that the main phase constituents of the laser-deposited CrFeCoNiMoWC alloy are austenite solution and M(Cr,Fe)C. After FSP, the primary austenite and MC carbide

phases were retained in the CrFeCoNiMoWC alloy despite the FSP rotary speeds. However, some new phases of WC and Co$_3$W were presented in the FSP plastic layer. Besides, the diffraction peak intensities of WC and Co$_3$W increased with the increase of the rotary speeds. During FSP, the tool material of WC-Co hard alloy was subjected to a strong thermal-mechanical coupling effect; thus, the tool was easily worn off[35] and then squeezed into the CrFeCoNiMoWC alloy, forming the as-received composite surface layer.

Figure 5 shows the SEM images taken from the cross section of the CrFeCoNiMoWC HEA layer prepared by LMD and FSP with a rotary speed of 300 rpm. Similar to other friction stir processed alloys,[13,36,37] three typical zones, the plastic zone (usually called the stir

zone) at the top surface with a thickness of about 40 μm, the thermomechanical effect zone, and the original laser-solidified zone, were recognized in the HEA prepared by FSP. In the plastic zone, the material was stirred by the WC-Co tool and subjected to the severest plastic deformation, inducing the temperature elevation to a high temperature of about 0.6 to 0.8 times the melting point.[38] Under the strong coupling effects of high temperature and shear strain, the microscaled LMD grain was broken into nanograins. Simultaneously, the continuous networks in the laser-melted microstructure were crushed into nanoparticles uniformly distributed in a disordered solid solution. The thermomechanical effect zone between the plastic zone and laser-solidified zone experienced the coupled fields of stress and thermal during the FSP process, which were lower than those in the plastic zone. Thus, the grains in the thermomechanical effect zone were deformed but not transformed into nanostructure. The laser-solidified microstructure below the thermomechanical effect region was not altered, because the FSP thermal and stress have little influence on it. To further observe the plastic zone, the FIB-TEM was used to identify the detailed microstructure, as shown in Figure 6. Similar to SEM images of the plastic zone, the laser-solidified dendritic with an average grain size of 3 to 4 μm was dramatically refined to about 5 to 100 nm (Figures 6(a), (c), and (e)). At the same time, the continuous networks of carbides and eutectic were broken into nanoparticles uniformly distributed in the refined austenite matrix. A great many subgrains and dislocations can be found in the TEM images. The ring-shaped selected area electron diffraction (SAED) image also indicates the nanograin formation at the
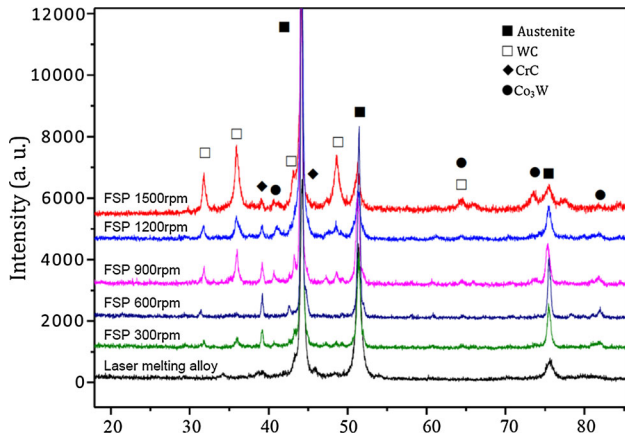

Fig. 4—XRD pattern of the laser-melting CrFeCoNiWMoMnC alloy layer before and after FSP with various rotary speeds.
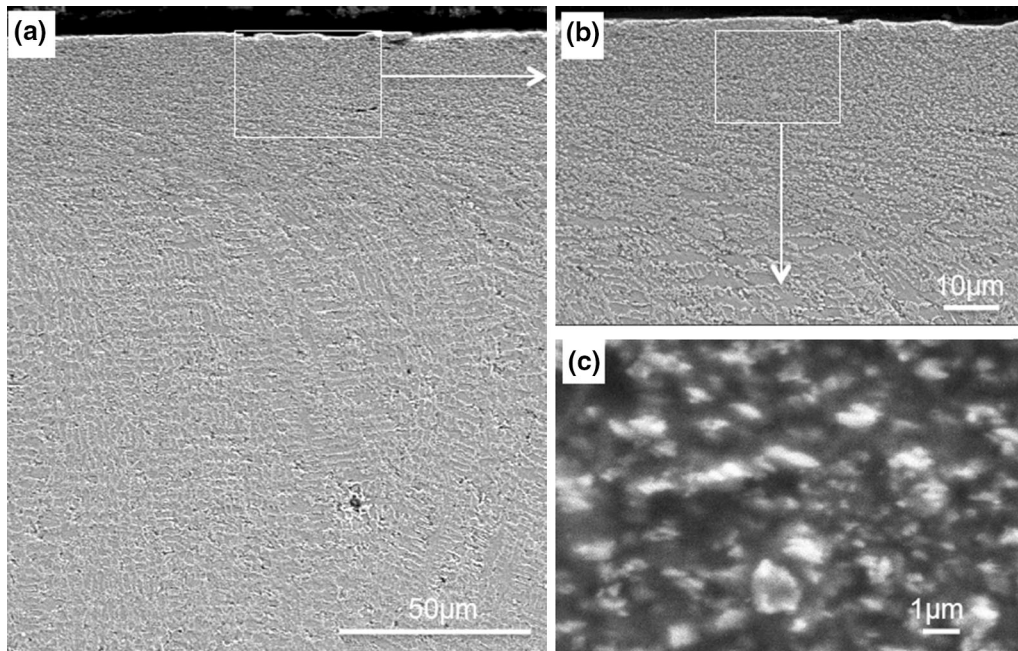

Fig. 5—SEM images taken from the cross section of the HEA layer after FSP with a rotary speed of 300 rpm: (a) showing three typical zones of plastic, thermomechanical, and solidified; (b) showing the plastic zone; and (c) high magnification of (b) showing the nanograin in the plastic zone.
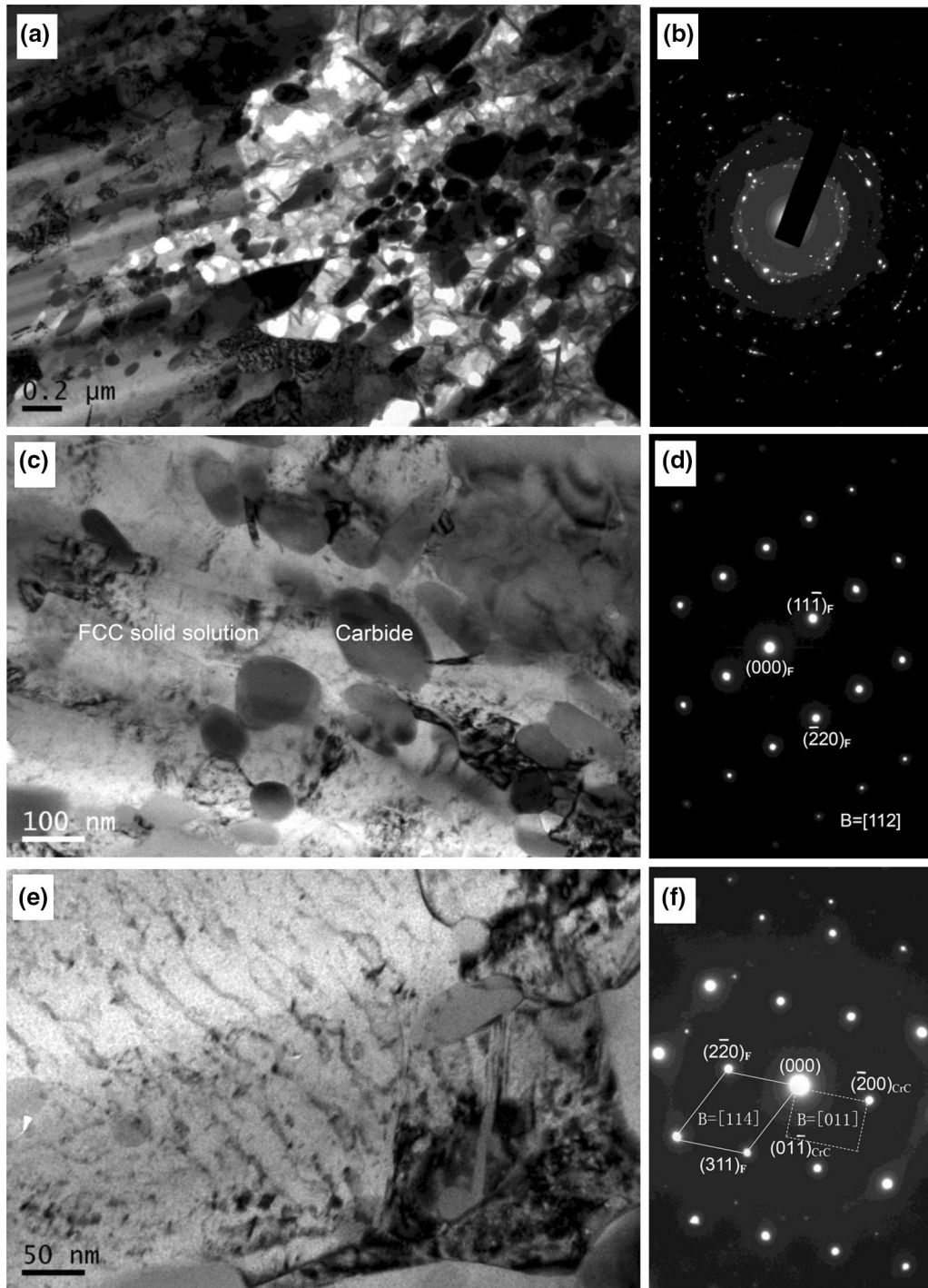
Fig. 6—(*a*), (*c*), and (*e*) TEM bright-field images of the plastic zone showing nanostructured CrFeCoNiWMoMnC surface layer processed at an FSP rotary speed of 300 rpm; (*b*), (*d*), and (*f*) their corresponding SAED patterns.

plastic zone (Figure 6(b)). The fcc phase can be observed in the SAED image with a zone axis of [112] (Figure 6(d)). Austenite and CrC phases can be detected in a coexisting SAED image (Figure 6(f)). Figure 7(a) shows the deformation nanotwins and corresponding diffraction pattern of the plastic zone. A bunch of twin lamellar structures with thickness of about 20 nm passing through a whole individual grain are observed

after FSP. Some of the boundaries of deformation twin or matrix lamellae are fuzzy owing to the interactions between dislocations and twin boundaries (TBs) and the activation or propagation of dislocations in the twins.[39] It is suggested that the TB stems from the GB. A corresponding SAED pattern exhibits the $\{\bar{1}\bar{1}1\}$ type twin, as marked in Figure 7(b). Overall twinning acts as an important deformation mechanism, leading to
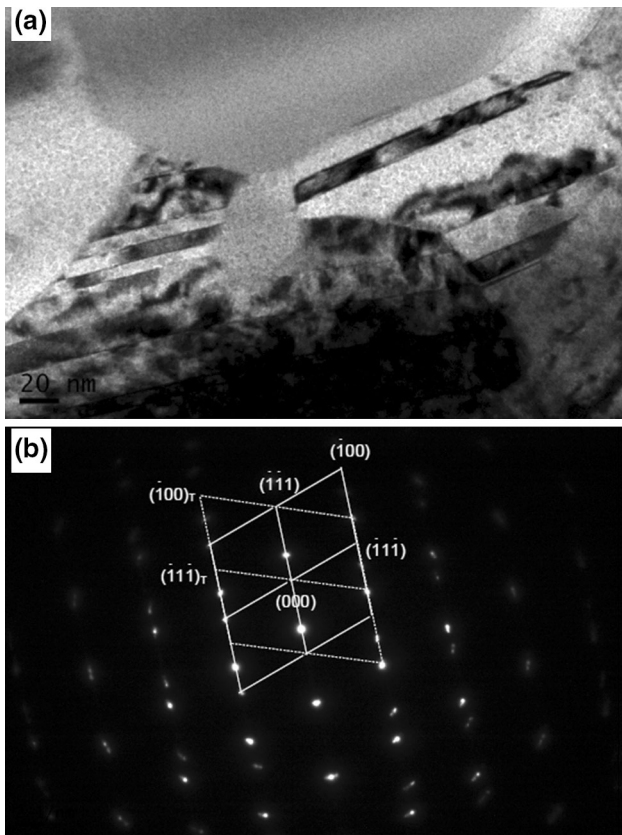
Fig. 7—TEM bright-field images showing the deformation nanotwins (*a*) and corresponding diffraction pattern (*b*) of the plastic zone.
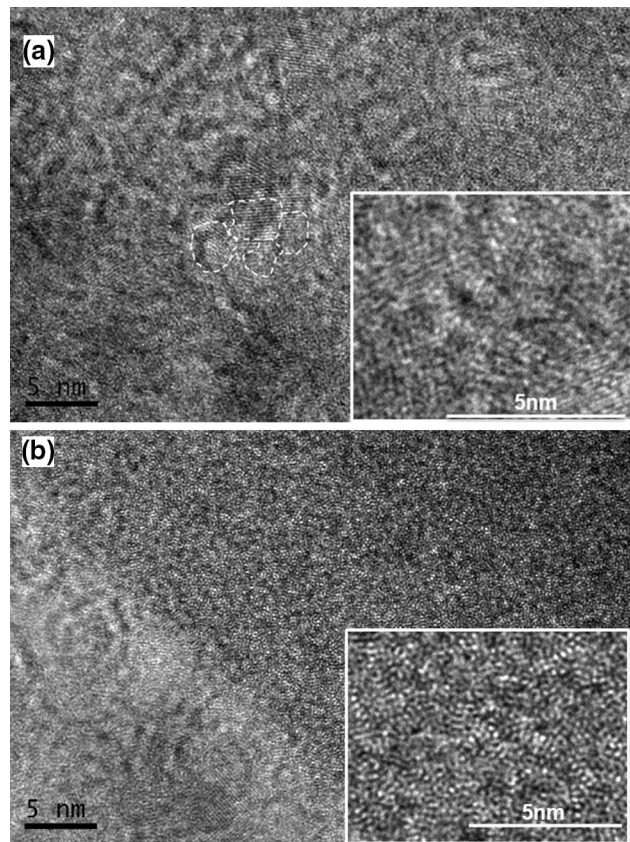
Fig. 8—HRTEM showing the formations of (*a*) nanograin and (*b*) amorphous in the plastic zone.

effective grain refinement. HRTEM was then conducted to observe the plastic zone, as presented in Figure 8. This process also confirmed that the laser-solidified grain was refined into nanograins, with part of the grain size below 5 nm (Figure 8(a)), even the amorphous formation (Figure 8(b)). The formation of amorphous was also observed in friction welding during which the material experienced the severest plastic deformation.[40]

The microstructural evolution was also influenced by the FSP rotary speed. When a high rotary speed of 900 rpm was applied, a different microstructure was observed, as presented in Figure 9, with the existence of three typical zones of plastic, thermomechanical, and original laser solidified. The thickness of the plastic zone increased to 130 μm (Figure 9(a)) compared with the plastic thickness of 40 μm at a lower rotary speed of 300 rpm (Figure 5(a)). In the plastic zone, the continuous networks were crushed into nanostructures, within which nanoparticles were uniformly distributed (Figures 9(b) and (c)). The WC-Co layer can also be found at the top of the plastic zone (Figure 9(d)), which was evidenced by EDS analysis. During the FSP process, the HEA sample reached a high temperature and was softened quickly under strong friction heat. In such circumstances, the FSP tool material was worn and formed a nanostructured WC-Co layer (Figure 9(e)) with thickness of about 25 μm, which ultimately bonded together with the plastic zone of the HEA and reserved at the top surface. Below the WC-Co layer, the

nanostructured HEA layer was presented (Figure 9(f)). On the whole, when a higher rotary speed of 900 rpm was used, the plastic thickness increased apparently and the WC-Co layer occurred locally.

With the further increase of the FSP rotary speed to 1200 rpm, the plastic zone became thicker, apparently with a thickness of about 350 μm, as evidenced in Figure 10. Interestingly, at the top surface of the plastic zone, the WC-Co layer thickness of about 50 to 200 μm exhibited complex spirals and vortex shapes (Figure 10(a)). Moreover, the WC-Co layer connected below the plastic zone with interlocking bonding, which was favorable for their connection. With a high-magnification SEM, the WC-Co was also changed into nanograin, owing to its co-deformation with CrFeCo NiMoWC alloy (Figure 10(b)). Similar to other FSP rotary speeds, the high magnification of the plastic zone showed a nanostructure with dispersive nanoparticles. The total thicknesses of both the plastic zone and the WC-Co layer increased with an increase of rotary speed.

When the FSP rotary speed increased to 1500 rpm, the plastic zone enlarged to about 400 μm, with a WC-Co layer of 50 to 100 μm, as shown in Figure 11. Similar to microstructures obtained at other rotary speeds, the WC-Co layer (Figure 11(b)) and plastic zone (Figure 11(c)) were transformed into nanostructures. The stirring speed affects heat input, and increasing the rotational speed leads to higher FSP temperatures. Therefore, with the increase of FSP rotary speed, the
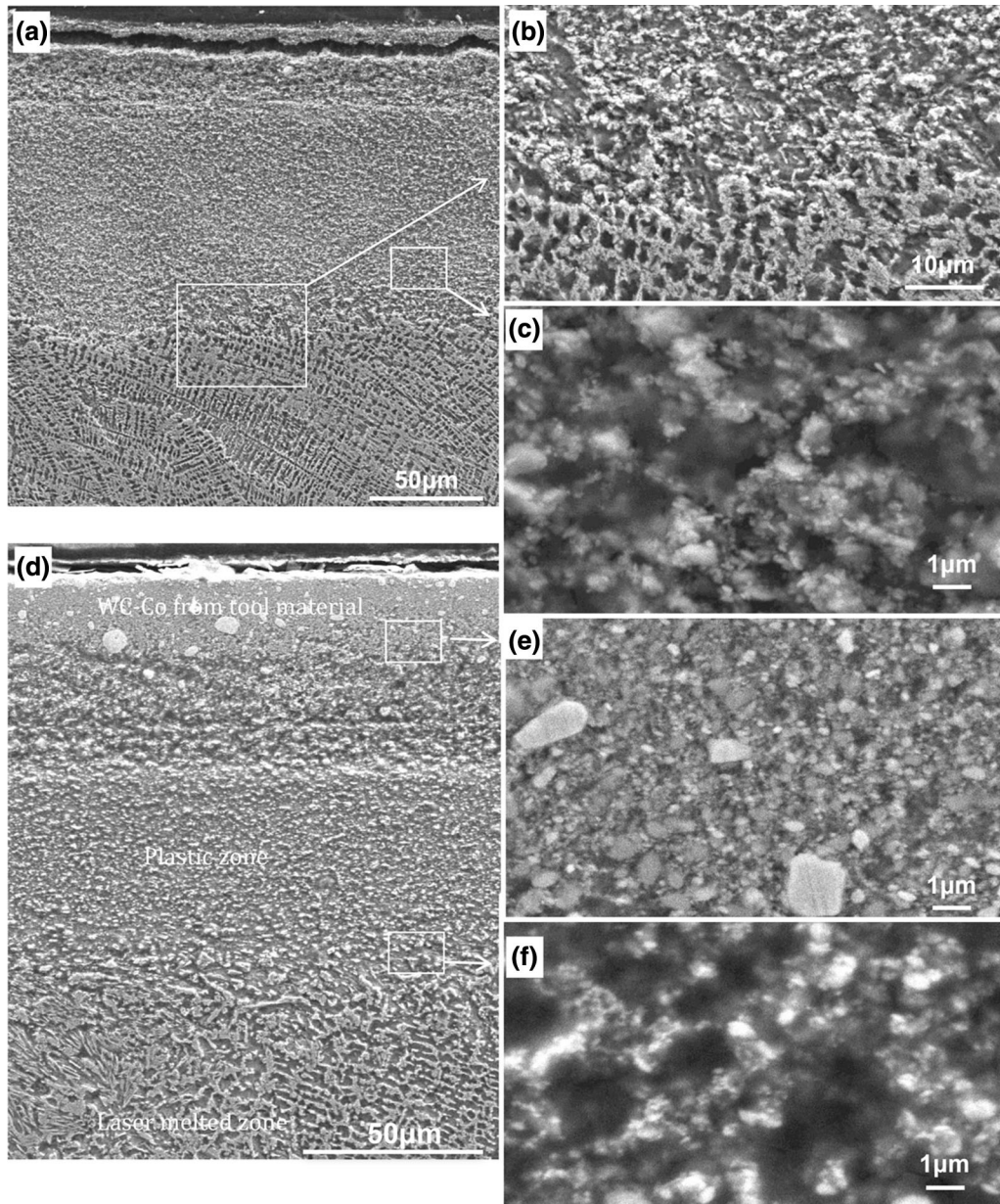
Fig. 9—SEM images taken from the cross section of the HEA layer after FSP with a rotary speed of 900 rpm: (*a*) low magnification, (*b*) high magnification showing the interface of the thermomechanical and laser-solidified zone, (*c*) high magnification showing the nanograin in the plastic zone, (*d*) low magnification showing the cohered WC-Co, (*e*) high magnification showing the WC-Co layer, and (*f*) high magnification showing the nanograin in the plastic zone.

plastic thickness of the CrFeCoNiMoWC alloy became thicker gradually with more bonded WC-Co material.

C. Effect of FSP on Properties of LMD CrFeCoNiMoWC Alloy

The microhardness for CrFeCoNiMoWC alloy before and after FSP is shown in Figure 12. It was obvious that the hardness was enhanced by FSP on LMD CrFeCoNi MoWC alloy. Moreover, a higher rotary speed, to some degree, can produce a higher hardness. The HEA was strengthened by mechanisms of twinning strengthening,

working hardening, dispersion strengthening, refinement strengthening, and dislocation strengthening.

Figure 13 shows the potentiodynamic polarization curves of the HEA process before and after FSP. It can be seen that the FSP parameter has an obvious influence on the corrosion resistance of HEA. Generally, the corrosion resistances became better after FSP. With the increase of FSP rotary speed, the corrosion resistances were enhanced. In laser-solidified HEA, the microstructure contained primary austenite and continuous carbide phases, the potentials of which were different. The continuous network of the carbide at the GBs promoted
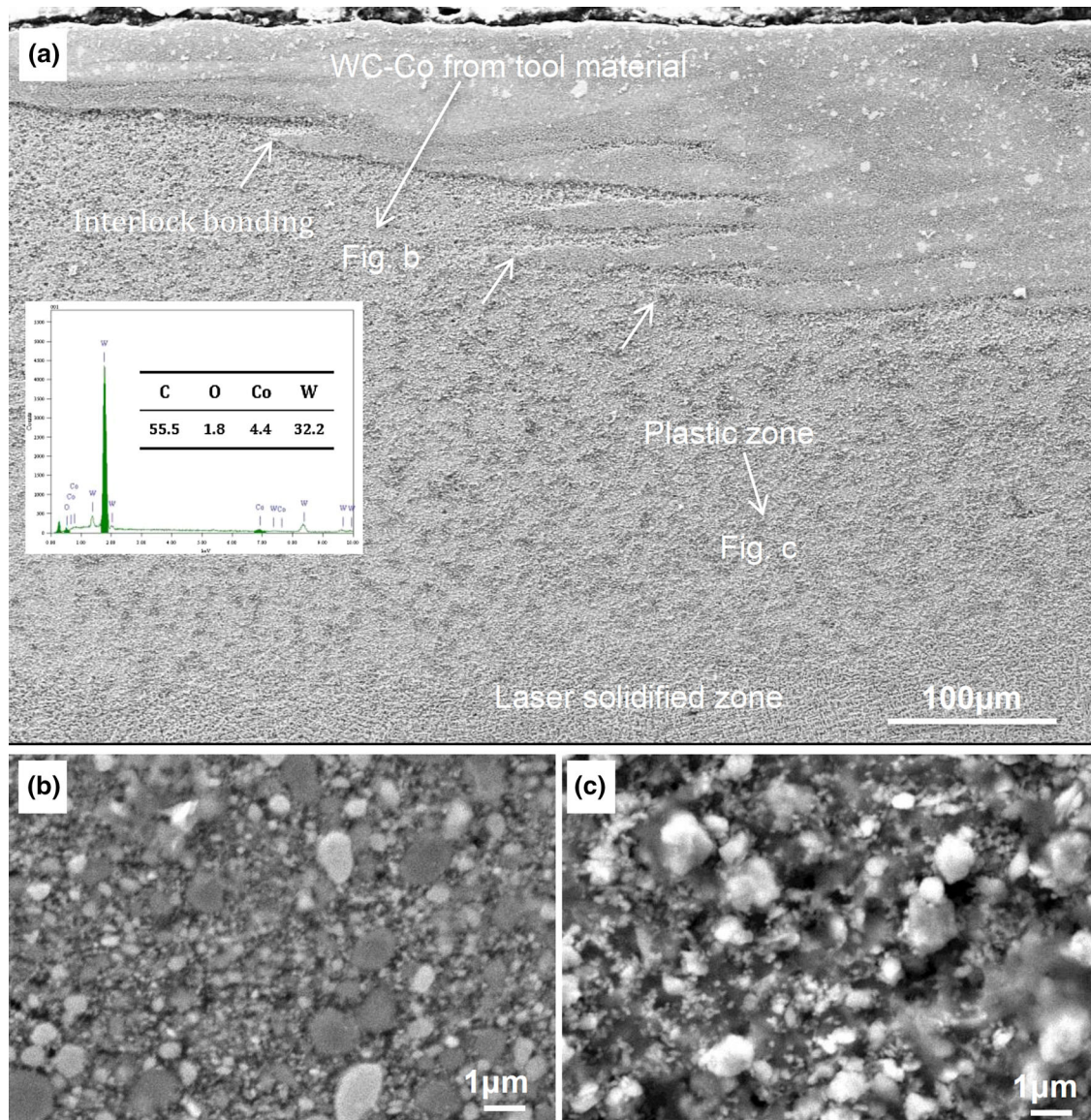
C	O	Co	W
55.5	1.8	4.4	32.2

Fig. 10—SEM images taken from the cross section of the HEA layer after FSP with a rotary speed of 1200 rpm: (*a*) low magnification, (*b*) high magnification showing the WC-Co layer, and (*c*) high magnification showing the nanograin in the plastic zone.

the corrosion. After FSP, the continuous network of carbide at GBs was not observed due to the breakage and partial dissolution of the carbide particles. Besides, the primary austenite phase was refined to nanograin and the continuous network of carbide was crushed to nanoparticles inside the grains rather on the boundaries after FSP. The redistribution of the carbide precipitates was favorable for their chemical corrosion property.

D. *Plastic Formation Mechanism During the Nanograin Formation Process*

The grain refinement mechanisms in the present study contain grain fragmentation and recrystallization nucleation, as schematically illustrated in Figure 14. First, under the heavy stress of FSP, the grain of laser solidification can be easily broken into small grain or subgrain by dislocation glide or twinning.[41,42] Second,

during the FSP process, the dynamic recrystallization occurs and dramatically refines the microstructure by dynamic balance of severe strain and restoration with mechanisms of well-known "strain-induced grain boundary migration" or the bulging processing.[12] Moreover, the amorphous was found in a local position of the plastic zone, owing to the special physical conditions, such as high temperature, high hydrostatic pressure, and large shear stress.[43]

At the preliminary stage of the FSP, with the breaking of the microscaled grain into nanograin or amorphous, the rate of dislocation generation is higher than the rate of dislocation annihilation, inducing a large number of dislocations.[44] However, a high density of dislocations within the nanograin is unstable and prone to glide toward the GB and then disappear when an external stress could enable the dislocation slip,[44] as reported by molecular dynamics simulations.[45] Therefore, with the
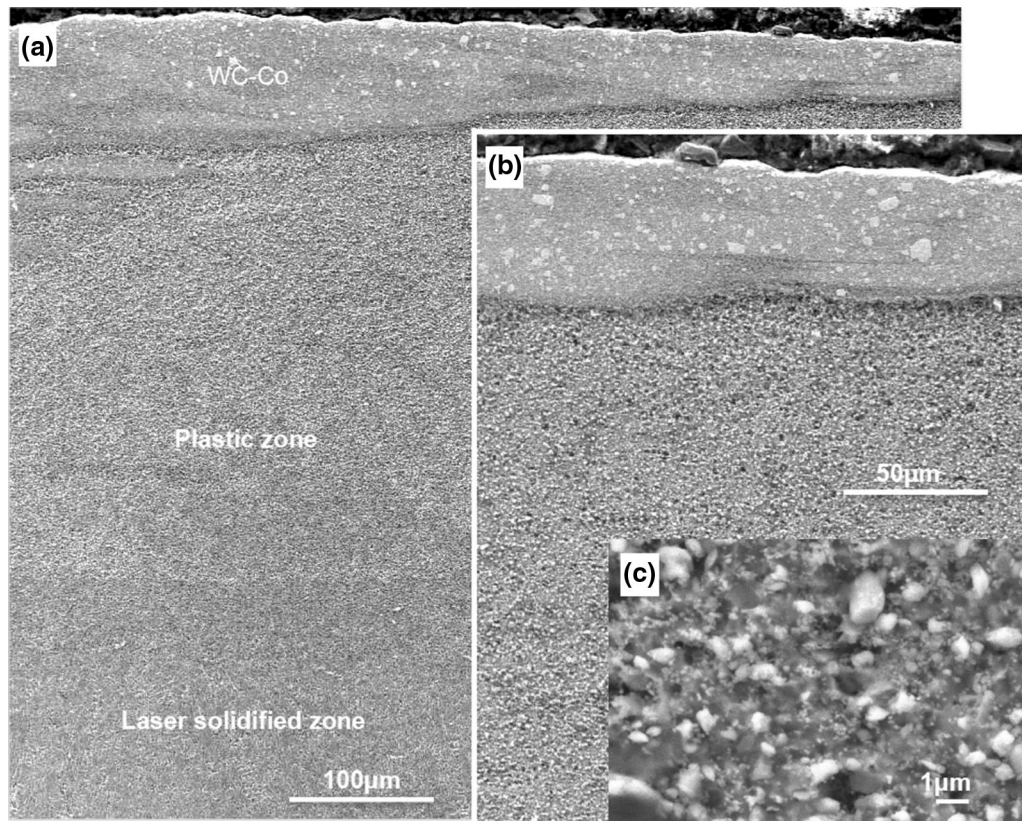
Fig. 11—SEM images taken from the cross section of the HEA layer after FSP with a rotary speed of 1500 rpm: (*a*) low magnification, (*b*) high magnification of (*a*) showing the WC-Co layer and plastic zone, and (*c*) high magnification showing the nanograin in the plastic zone.
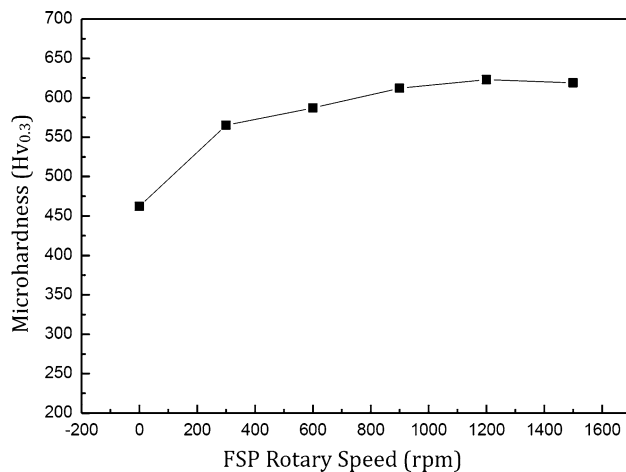

Fig. 12—Vickers 0.3 microhardness of the HEA before and after FSP.

further deformation of FSP, the dislocations tend to vanish at GBs.[40] This seems to be the case in the FSP deformation process of CrFeCoNiMoWC in the present study, which includes amorphous and nanograin. Therefore, the dislocation behaviors are considered to be important in the understanding of deformation mechanisms. The high density of dislocations on two intercrossing {111} planes can easily lead to the formation of Lomer–Cottrell (L–C) locks,[46] which occur by the reaction of two leading partials from two dissociated lattice dislocations and two intersecting slip planes.[44] A typical HRTEM image of the plastic zone showing the L–C lock formation is presented in Figure 15. The two {111} groups can be indexed as $(1\bar{1}1)$ and $(\bar{1}11)$, and the $\langle 110 \rangle$ direction is $[\bar{1}10]$ in the image. A lattice dislocation in the fcc crystal is usually decomposed into two $1/6\langle 112 \rangle$ type partial dislocations. For instance,[44] a lattice dislocation of $1/2[0\bar{1}\bar{1}]$ at plane $(1\bar{1}1)$ is decomposed into $1/6[1\bar{1}\bar{2}] + 1/6[1\bar{2}1]$. Meanwhile the lattice dislocation of $1/2[101]$ at plane $(\bar{1}11)$ is decomposed into $1/6[211] + 1/6[1\bar{1}\bar{2}]$. When the two full dislocations meet at the junction of $(1\bar{1}1)$ and $(\bar{1}11)$, the dislocation reaction of $1/6[1\bar{2}\bar{1}] + 1/6[211] \rightarrow 1/6[1\bar{1}0]$ occurs, which represents the two leading partials transformed into a stair-rod dislocation. In combination with the other two partial dislocations, the L–C lock structure formed. Because the L–C lock structure is extended on two {111} planes, it hinders the dislocation glide and accumulates dislocations.[46] The occurrence of high-density L–C locks hinders the motion of dislocations dramatically, leading to the increase of dislocation density; thus, the strength of the plastic zone is enhanced.

The strength of nanostructured materials relies on dislocations, GBs, and TBs. TBs not only barrier dislocation motion but also restrict dislocation nucleation and accumulation, which are favorable for both

strength and ductility.[47] Therefore, studying the interactions between dislocations and TBs is considered to be important. Figure 16 shows an HRTEM image of the dislocation configuration when a full dislocation interacts with a partial dislocation at a TB. It can be seen that the TB at the left does not lie on the same atomic plane as the TB at the right side, showing a step along the TB. When the TB plane extends from left to right, the step has a height of two {111} atomic planes. When extending the TB plane from the right to left, the step shows a height of one {111} atomic plane. The discrepancy is due to the full dislocation. When a full dislocation moves to the TB step, it can react with the partial dislocation that forms a step in the TB; thus, movement of the full dislocation is inhibited at the step. The full dislocation may be pinned and interacts with the twinning or detwinning partial at the step, hindering the partial dislocation glide along the TB. In order to discuss the dislocation-TB interactions, the double Thompson tetrahedron was introduced, as illustrated in Figure 17. The Thompson tetrahedron above the (111) TB represents the slip systems in the matrix, and the bottom tetrahedron represents the slip systems of the twin.[47–49] The Burgers vectors of **AB**, **BC**, **CA**, **Aδ**, **Bδ**,

and **Cδ** could slip in the matrix and twin. For instance, when a full dislocation **DA** that contains a leading partial **Dγ** and a trailing partial **γA** reacts with a partial dislocation **Aδ**, a Frank sessile dislocation **Dδ** tends to form, which can be illustrated as follows:

$$\gamma A + \delta B \rightarrow \delta\gamma/BA \qquad [1]$$

$$DA + A\delta \rightarrow D\delta \qquad [2]$$
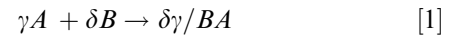
It should be noted that the energy variation of the preceding reaction is negative, thus favoring the spontaneous occurrence. Consequently, when a full dislocation moves to a TB step, it tends to interact with the twinning partial and yield a sessile dislocation rather than totally or partially pass through the TB. The sessile dislocation thus improves the strength of the nanostructured HEA.

Figure 18 shows an HRTEM image of the accumulation of a high density of dislocations at the TB with TBs, stacking faults (SFs), and GBs. The grain rotation can also be found in the image. It can be found that the accumulation of a high density of dislocations at the TB triggered secondary twins and SFs *via* the emission of
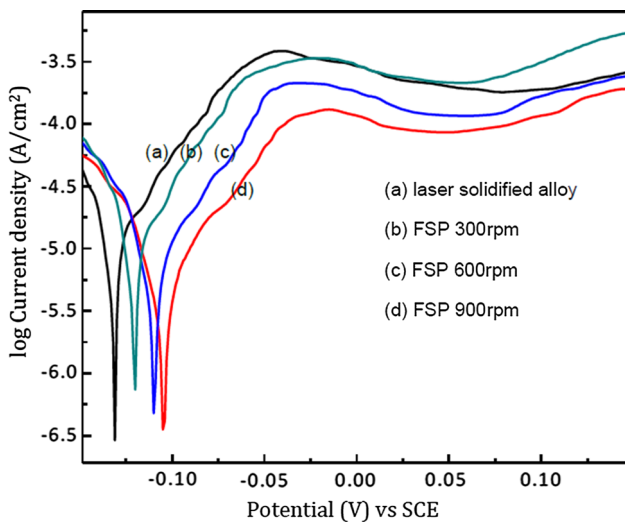

Fig. 13—Potentiodynamic polarization curves of the HEA process at different FSP rotary speeds.
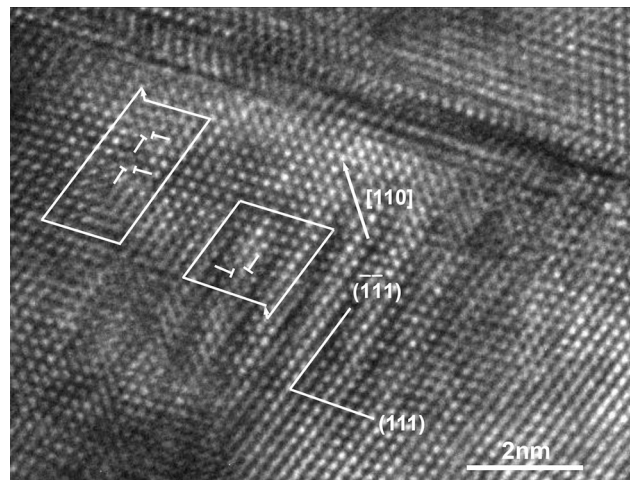

Fig. 15—HRTEM image showing the formation of L–C locks with two (111) planes marked by white lines and Burgers circuits drawn in the image.
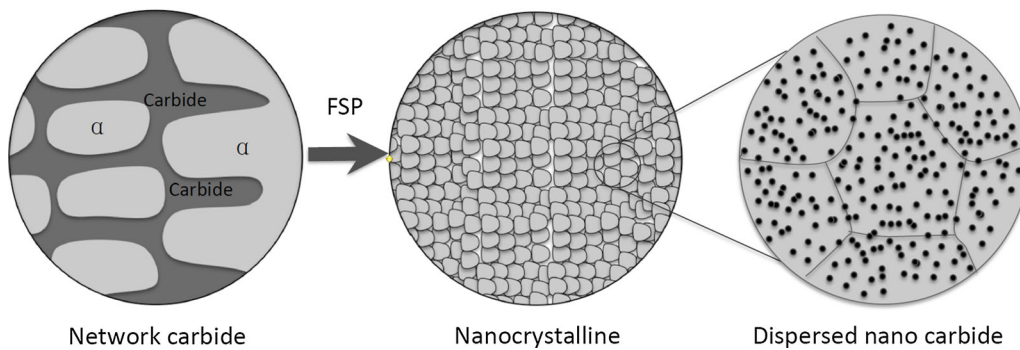

Fig. 14—Schematic illustration of the grain refinement process of the HEA during FSP.

partial dislocations to release the local stress concentration in the zone with disordered TB. It is reasonable to propose that when a high density of dislocations accumulate and tangle at the TB, secondary twins and SFs can be activated *via* emission of partial dislocation in the disordered area to alleviate the stress concentration. Deformation twinning and dislocation slip tend to occur during FSP of CrFeCoNiMoWC, playing an important role in the dislocation-TB interactions and nanograin formation.

IV. CONCLUSIONS

The fabrication process of the CrFeCoNiMoWC HEA by LMD and FSP was carried out. The microstructural evolution and deformation mechanism were studied. The results are summarized as follows:

1. The microstructures of the laser-melted CrFeCoNiMoWC alloy are mainly composed of dendritic and subeutectic structures with grain sizes of about 3 to 4 μm. The interdendritic eutectic formed a continuous structure along the GB. The main phases were austenite solution and M(Cr,Fe)C.

2. The nanostructured plastic zone with a grain size 5 to 100 nm can be found, and the continuous networks were crushed into nanoparticles uniformly distributed in austenite solution after FSP. The primary austenite and MC carbide phases were retained despite the FSP rotary speeds, while new phases of WC and Co_3W were generated in the plastic zone due to the worn debris of the FSP tool. Moreover, the more rapid FSP rotary speed enables the higher heat input and temperature, which ultimately results in a much thicker plastic zone and WC-Co layer.

3. After FSP, the microhardness of the plastic zone was improved and a higher rotary speed could produce a higher hardness to some degree. The strengthening mechanisms include working hardening, dispersion strengthening, refinement strengthening, twinning strengthening, and dislocation strengthening. Moreover, the FSP can also improve its electrochemical
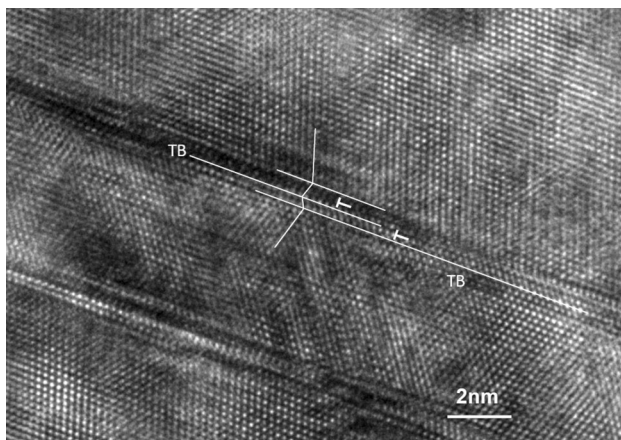

Fig. 16—HRTEM image of the dislocation configuration when a full dislocation interacts with a partial dislocation at a TB.
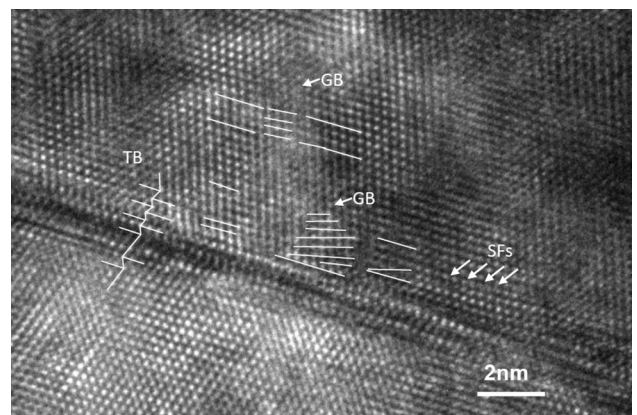

Fig. 18—HRTEM image showing the accumulation of a high density of dislocation at the TB with TBs, SFs, and the GB marked in the image.
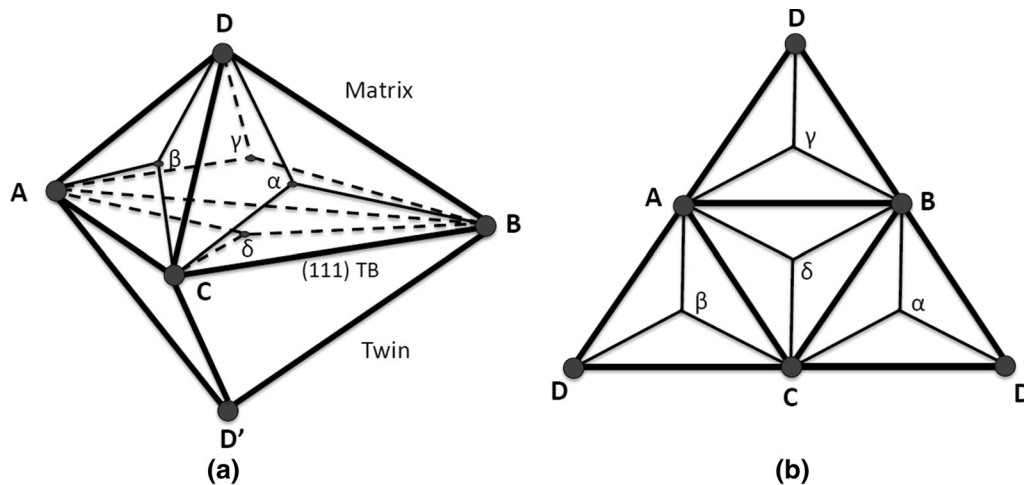

Fig. 17—(*a*) Diagrammatic sketch of a double Thompson tetrahedron and (*b*) its two-dimensional representation of the top tetrahedron.

corrosion property due to the breakage and partial dissolution of the carbide particles.

4. Interestingly, the amorphous is found in the plastic zone, owing to the high temperature, high hydrostatic pressure, and large shear stress during FSP. The dislocation behaviors in the FSP deformation process are also analyzed. The HRTEM shows the formation of the L–C lock, the dislocation configuration of a full dislocation interacting with a partial dislocation at a TB, and the high density of dislocation at TB with TBs, SFs, and GB in the plastic zone, which can hinder the motion of dislocations and account for the increase of strength.

REFERENCES

1. J. Frontan, Y. Zhang, M. Dao, J. Lu, F. Galvez, and A. Jerusalem: *Acta Mater.*, 2012, vol. 60, pp. 1353–67.
2. K. Lu: *Science*, 2014, vol. 345, pp. 1455–56.
3. X.C. Liu, H.W. Zhang, and K. Lu: *Science*, 2013, vol. 342, pp. 337–40.
4. D. Geist, C. Rentenberger, and H.P. Karnthaler: *Acta Mater.*, 2011, vol. 59, pp. 4578–86.
5. M. Ruppert, C. Schunk, D. Hausmann, H.W. Hoeppel, and M. Goeken: *Acta Mater.*, 2016, vol. 103, pp. 643–50.
6. J. Moering, X. Ma, G. Chen, P. Miao, G. Li, G. Qian, S. Mathaudhu, and Y. Zhu: *Scripta Mater.*, 2015, vol. 108, pp. 100–03.
7. Y. Huang, L. Wan, S. Lv, H. Liu, and J. Feng: *Mater. Design*, 2013, vol. 52, pp. 821–27.
8. W.L. Li, N.R. Tao, and K. Lu: *Scripta Mater.*, 2008, vol. 59, pp. 546–49.
9. R.A. Seraj, A. Abdollah-Zadeh, M. Hajian, F. Kargar, and R. Soltanalizadeh: *Metall. Mater. Trans. A*, 2016, vol. 47A, pp. 3564–72.
10. A. Tripathi, A. Tewari, A.K. Kanjarla, N. Srinivasan, G.M. Reddy, S.M. Zhu, J.F. Nie, R.D. Doherty, and I. Samajdar: *Metall. Mater. Trans. A*, 2016, vol. 47A, pp. 2201–16.
11. J. Qian, J. Li, J. Xiong, F. Zhang, and X. Lin: *Mater. Sci. Eng. A*, 2012, vol. 550, pp. 279–85.
12. R. Li, T. Yuan, Z. Qiu, K. Zhou, and J. Li: *Surf. Coat. Technol.*, 2014, vol. 258, pp. 415–25.
13. Y. Morisada, H. Fujii, T. Mizuno, G. Abe, T. Nagaoka, and M. Fukusumi: *Mater. Sci. Eng. A*, 2009, vol. 505, pp. 157–62.
14. Y. Morisada, H. Fujii, T. Mizuno, G. Abe, T. Nagaoka, and M. Fukusumi: *Surf. Coat. Technol.*, 2011, vol. 205, pp. 3397–3403.
15. L.J. Santodonato, Y. Zhang, M. Feygenson, C.M. Parish, M.C. Gao, R.J.K. Weber, J.C. Neuefeind, Z. Tang, and P.K. Liaw: *Nat. Commun.*, 2015, vol. 6.
16. Z. Li, K.G. Pradeep, Y. Deng, D. Raabe, and C.C. Tasan: *Nature*, 2016, vol. 534, p. 227.
17. Y. Liu, S. Ma, M.C. Gao, C. Zhang, T. Zhang, H. Yang, Z. Wang, and J. Qiao: *Metall. Mater. Trans. A*, 2016, vol. 47A, pp. 3312–21.
18. C. Varvenne, A. Luque, and W.A. Curtin: *Acta Mater.*, 2016, vol. 118, pp. 164–76.
19. Y. Zhang, T.T. Zuo, Z. Tang, M.C. Gao, K.A. Dahmen, P.K. Liaw, and Z.P. Lu: *Progr. Mater. Sci.*, 2014, vol. 61, pp. 1–93.
20. B. Song, S. Dong, and C. Coddet: *Scripta Mater.*, 2014, vol. 75, pp. 90–93.
21. B. Song, S. Dong, S. Deng, H. Liao, and C. Coddet: *Optic Laser Technol.*, 2014, vol. 56, pp. 451–60.
22. R. Li, Y. Shi, Z. Wang, L. Wang, J. Liu, and W. Jiang: *Appl. Surf. Sci.*, 2010, vol. 256, pp. 4350–56.
23. R. Li, J. Liu, Y. Shi, L. Wang, and W. Jiang: *Int. J. Adv. Manuf. Technol.*, 2012, vol. 59, pp. 1025–35.
24. C. Huang, Y. Zhang, J. Shen, and R. Vilar: *Surf. Coat. Technol.*, 2011, vol. 206, pp. 1389–95.
25. T.M. Yue and H. Zhang: *Mater Res. Innov.*, 2014, vol. 182, pp. 624–28.
26. T.M. Yue, H. Xie, X. Lin, H.O. Yang, and G.H. Meng: *J. Alloys Compd.*, 2014, vol. 587, pp. 588–93.
27. K.J. Huang, X. Lin, Y.Y. Wang, C.S. Xie, and T.M. Yue: *Mater. Res. Innov.*, 2014, vol. 182, pp. 1008–11.
28. X. Ji, H. Duan, H. Zhang, and J. Ma: *Tribol. Trans.*, 2015, vol. 58, pp. 1119–23.
29. B. Schuh, F. Mendez-Martin, B. Voelker, E.P. George, H. Clemens, R. Pippan, and A. Hohenwarter: *Acta Mater.*, 2015, vol. 96, pp. 258–68.
30. Q.H. Tang, Y. Huang, Y.Y. Huang, X.Z. Liao, T.G. Langdon, and P.Q. Dai: *Mater. Lett.*, 2015, vol. 151, pp. 126–29.
31. H. Yuan, M. Tsai, G. Sha, F. Liu, Z. Horita, and Y. Zhu: *J. Alloys Compd.*, 2016, vol. 686, pp. 15–23.
32. X. Zhao, B. Song, W. Fan, Y. Zhang, and Y. Shi: *J. Alloys Compd.*, 2016, vol. 665, pp. 271–81.
33. H. Yan, P. Zhang, Z. Yu, C. Li, and R. Li: *Optic Laser Technol.*, 2012, vol. 44, pp. 1351–58.
34. H. Yan, A. Wang, K. Xu, W. Wang, and Z. Huang: *J. Alloy Compd.*, 2010, vol. 505, pp. 645–53.
35. S.R. Nathan, V. Balasubramanian, S. Malarvizhi, and A.G. Rao: *Int. J. Refract. Meth. H*, 2016, vol. 56, pp. 18–26.
36. Y. Morisada, H. Fujii, T. Mizuno, G. Abe, T. Nagaoka, and M. Fukusumi: *Surf. Coat. Technol.*, 2009, vol. 204, pp. 386–90.
37. H. Peng, R. Lia, T. Yuan, H. Wu, and H. Yan: *J. Mater. Res.*, 2015, vol. 30, pp. 717–26.
38. J. Qian, J. Li, F. Sun, J. Xiong, F. Zhang, and X. Lin: *Scripta Mater.*, 2013, vol. 68, pp. 175–78.
39. G. Liu, J. Gu, S. Ni, Y. Liu, and M. Song: *Mater. Charact.*, 2015, vol. 103, pp. 107–19.
40. S. Fukumoto, H. Tsubakino, K. Okita, M. Aritoshi, and T. Tomita: *Scripta Mater.*, 2000, vol. 42, pp. 807–12.
41. P. Xue, B.L. Xiao, and Z.Y. Ma: *Scripta Mater.*, 2013, vol. 68, pp. 751–54.
42. M.H. Razmpoosh, A. Zarei-Hanzaki, S. Heshmati-Manesh, S.M. Fatemi-Varzaneh, and A. Marandi: *J. Mater. Eng. Perform.*, 2015, vol. 24, pp. 2826–35.
43. P. Liu and Q. Shi: *Phil. Mag. Lett.*, 2015, vol. 95, pp. 312–18.
44. S. Ni, Y.B. Wang, X.Z. Liao, S.N. Alhajeri, H.Q. Li, Y.H. Zhao, E.J. Lavernia, S.P. Ringer, T.G. Langdon, and Y.T. Zhu: *Scripta Mater.*, 2011, vol. 64, pp. 327–30.
45. J. Schiotz and K.W. Jacobsen: *Science*, 2003, vol. 301, pp. 1357–59.
46. J.H. Lee, T.B. Holland, A.K. Mukherjee, X. Zhang, and H. Wang: *Sci. Rep.*, 2013, vol. 3.
47. S. Ni, Y.B. Wang, X.Z. Liao, R.B. Figueiredo, H.Q. Li, S.P. Ringer, T.G. Langdon, and Y.T. Zhu: *Acta Mater.*, 2012, vol. 60, pp. 3181–89.
48. Y.T. Zhu, X.Z. Liao, and X.L. Wu: *Progr. Mater. Sci.*, 2012, vol. 57, pp. 1–62.
49. Y.T. Zhu, X.L. Wu, X.Z. Liao, J. Narayan, L.J. Kecskes, and S.N. Mathaudhu: *Acta Mater.*, 2011, vol. 59, pp. 812–21.